Multilevel Fast Multipole Algorithm for Fields

Diego M. Solís[a], Marta G. Araújo[a,*], Santiago García[b], Fernando Obelleiro[a] and José M. Taboada[c]

[a]*Department of Signal and Communication Theory, E.E. Telecomunicación, Universidade de Vigo, 36310 Vigo, Spain* (dmartinezsolis@gmail.com, martaga@com.uvigo.es, obi@com.uvigo.es)

[b]*Electromagnetics Measurements Center (CEMEDEM) of Spanish Navy, Escuela Naval Militar, 36920 Marín, Spain* (santiagogarcia@fn.mde.es)

[c]*Department of Computers and Communications Technology, Escuela Politécnica, Universidad de Extremadura, 10003 Cáceres, Spain* (tabo@unex.es)

Corresponding author: *martaga@com.uvigo.es

Acknowledgements

This work was supported by the European Regional Development Fund (ERDF) and the Spanish Government, Ministerio de Economía y Competitividad, Dirección General de Investigación Científica y Técnica (Projects MAT2014-58201-C2-1-R, MAT2014-58201-C2-2-R), from the ERDF and the Galician Regional Government under agreement for funding the Atlantic Research Center for Information and Communication Technologies (AtlantTIC), and from the ERDF and the Extremadura Regional Government (Junta de Extremadura) under Project IB13185.

Multilevel Fast Multipole Algorithm for Fields

Abstract: An efficient implementation of the multilevel fast multipole algorithm (MLFMA) is herein applied to accelerate the calculation of the electromagnetic near- and far-fields after the equivalent surface currents have been obtained. In spite of all the research efforts being drawn to the latter, the electric and/or magnetic fields (or other parameters derived from these) are ultimately the magnitudes of interest in most of the cases. Though straightforward, their calculation can be computationally demanding, and hence the importance of finding a sped-up accurate representation of the fields via a suitable setup of the method. A complete self-contained formulation for both near- and far-fields and for problems including multiple penetrable regions is shown in full detail. Through numerical examples we show that the efficiency and scalability of the implementation leads to a drastic reduction of the computation time.

Keywords: Numerical integral methods; Method of Moments (MoM); Multilevel Fast Multipole Algorithm (MLFMA); Electromagnetic optics; Radiated fields.

1. Introduction

The widespread use of the multilevel fast multipole algorithm (MLFMA) [1–4] for the achievement of the rigorous solution of large-scale radiation and scattering electromagnetic problems is currently undeniable. The approach has been extensively applied to expedite the iterative resolution of the large and dense matrix systems resulting from the application of surface integral-equation (SIE) formulations and the method of moments (MoM) [5]. The combination with the latest advances in computer science has led to efficient parallel implementations that can deal with the solution of many real-world challenging problems [6–11]. Hence, the presence of MLFMA in very assorted and emerging fields is progressively greater due to the increasing scientific and industrial necessities that demand efficient computational solutions to many practical applications [12–26].

Otherwise, once the application of MLFMA provides the problem solution in the form of electric and/or magnetic equivalent currents distributed over the boundary surfaces and interfaces of the homogeneous or piece-wise homogeneous materials, a data post-processing is usually mandatory to obtain the proper results for each specific study. Remarkably, these subsequent computations involving the calculation of far and near field distributions often demand time and computational resources in the order of those required to solve the problem, or even higher in certain cases. Illustrative examples of highly demanding simulations in terms of post-processing computational cost can be found in many applications, from the

radiofrequency band, as the often requested computation of the bistatic radar cross section or the electromagnetic radiation in the vicinity of extremely large targets [10, 11], to nanoplasmonic biosensing applications in the optical range [17–26]. In [18, 25, 27], e.g., the authors have faced computational challenges related to the post-processing of the results when dealing with real-life nanophotonic applications. That post-processing would have been impossible without an accelerated computation generalized to multiregion scenarios, such as the implementation presented here.

This work clearly shows that MLFMA can be an efficient tool not only for the problem solving, but also to accurately and efficiently handle the computations that follow the equivalent currents finding, as it was briefly pointed out in [4]. The idea has also been previously explored in works [28, 29] for far- and near- field computations, respectively. Nevertheless, the novelty here lies in the fully detailed presentation of a complete self-contained formulation for the expedited computation of electromagnetic fields in the post-processing stage for problems including multiple penetrable regions. So, the first obvious advantage of our approach is that it is valid for all kind of homogeneous or piecewise homogeneous composite bodies with arbitrary materials involving open and/or closed surfaces. In [28], for instance, most of the attention is given to the parallelization strategy rather than the mathematics of the method itself, which by the way applies to perfect electric conductors only.

To illustrate the capabilities of the approach, a large-scale example in the emerging field of nanoplasmonics, consisting of a large assembly of nanoparticles, is considered in the numerical results section. The electric near field distribution, which is required for the calculation of the surface enhanced Raman scattering (SERS) [30, 31] is accurately and efficiently obtained by means of MLFMA. The SERS enhancement calculation is usually employed for the assessment of the sensing capabilities of nanoplasmonic systems. The differential scattering cross section of the array [32, 33] is also included for several planes. Both, SERS and differential scattering cross section, are challenging problems involving intensive near and far field hard computations. The results demonstrate that the use of MLFMA, together with an adequate implementation strategy, allows a dramatical reduction of the post-processing numerical cost.

2. MLFMA for computing radiated fields

Let us consider one or several homogeneous or piecewise homogeneous objects placed in a homogeneous (unbounded) medium. Based on Love's equivalence principle, the original problem can be expressed in terms of equivalent electric and magnetic currents placed over the boundary surfaces. A set of SIEs can be derived for the equivalent currents by imposing the continuity of the tangential components of the fields on the surfaces. The equivalent currents are expanded into a sum of known vector basis functions $\mathbf{f}_n$ in the form:

$$\mathbf{J}(\mathbf{r}) = \sum_n J_n \mathbf{f}_n \tag{1}$$

$$\mathbf{M}(\mathbf{r}) = \sum_n M_n \mathbf{f}_n, \tag{2}$$

where J_n and M_n are the unknown expansion complex coefficients. The conventional MoM formulation can be then applied, yielding a matrix system that can be solved directly or by accelerated techniques such as MLFMA in order to obtain the current coefficients.

Once the main problem has been solved and the current coefficients J_n and M_n are known, the calculation of output results still requires the computation of radiated/scattered electric and magnetic fields. Let us consider the calculation of these fields at the observation points **r** placed in region *i*, and let us denote with $\mathbf{J}_{ij}$ and $\mathbf{M}_{ij}$ the equivalent currents on the interface surfaces S_{ij} between adjacent regions *i* and *j*. The radiated/scattered fields can be straightforwardly obtained from the Straton-Chu formulas form the equivalent currents as:

$$\mathbf{E}(\mathbf{r}) = \sum_{j \in B_i} \left(-\eta_i \mathcal{L}_i(\mathbf{J}_{ij}) + \mathcal{K}_i(\mathbf{M}_{ij}) - \frac{1}{2} \hat{n}_{ij} \times \mathbf{M}_{ij} \right) \tag{3}$$

$$\mathbf{H}(\mathbf{r}) = \sum_{j \in B_i} \left(-\frac{1}{\eta_i} \mathcal{L}_i(\mathbf{M}_{ij}) - \mathcal{K}_i(\mathbf{J}_{ij}) + \frac{1}{2} \hat{n}_{ij} \times \mathbf{J}_{ij} \right), \tag{4}$$

where B_i are the indexes of the regions adjacent to region *i*, $\hat{\boldsymbol{n}}_{ij}$ is the unit vector normal to S_{ij} pointing toward region *i* and the following integro-differential operators have been defined:

$$\mathcal{L}_i(\mathbf{X}_{ij}) = jk_i \left[\int_S \mathbf{X}_{ij}(\mathbf{r}') G_i(\mathbf{r}, \mathbf{r}') dS' + \frac{1}{k_i^2} \nabla \int_S \nabla' \cdot \mathbf{X}_{ij}(\mathbf{r}') G_i(\mathbf{r}, \mathbf{r}') dS' \right] \tag{5}$$

$$\mathcal{K}_i(\mathbf{X}_{ij}) = \int_{S, PV} \mathbf{X}_{ij}(\mathbf{r}') \times \nabla G_i(\mathbf{r}, \mathbf{r}') dS', \tag{6}$$

where k_i is the wavenumber in region *i*, $\nabla' \cdot$ denotes the divergence in the primed (source) coordinates, $\mathbf{r}' \in S_{ij}$ and $G_i(\mathbf{r}, \mathbf{r}')$ is the homogeneous Green's function in region *i*. *PV* denotes the principal value of the integral in Eq. (6).

The application of MLFMA to compute electric and magnetic fields starts with the usual hierarchical decomposition of the geometry using octrees (for this decomposition we apply the highly efficient procedures described in [34]). However, in this case the multilevel octree encloses not only the geometry, but also the observation points at which the electromagnetic fields will be computed. It must be noted at this point that, in [29], the near-field post-processing phase splits the simulation domain, which only involves one scatterer, into two sub-domains: one with the scatterer and another with the observation points in the background medium. Our generalized approach, on the contrary, implements a hybridized octree addressing cells with either observation points, radiating current elements or both, each cell including as many regions as necessary. While of subtle nature, the difference in algorithmic structure is important, as the background medium and several interior regions from multiple scatterers can be framed within the same octree cell. The

electric near field for a given observation point $\mathbf{r}_f$ belonging to the region *i* and to the octree group *p* can be then expressed as:

$$\mathbf{E}(\mathbf{r}_f) = \sum_{j\in B_i}\sum_{q\in B_p}\sum_{\substack{n\in G_q \\ n\in S_{ij}}}\left(-\eta_i s_{ij}\mathcal{L}_i(\mathbf{f}_n)J_n + s_{ij}\mathcal{K}_i(\mathbf{f}_n)M_n - \frac{1}{2}\hat{n}_{ij}\times\mathbf{f}_n M_n\right) + \sum_{j\in B_i}\left(\frac{-jk_i}{4\pi}\right)^2\int_{S^2} e^{-j\mathbf{k}_i(\mathbf{r}_f-\mathbf{r}_p)}$$
$$\left[\eta_i\sum_{q\notin B_p}\alpha^i_{pq}\left(k_i,\mathbf{r}_{pq}\right)\sum_{\substack{n\in G_q \\ n\subset S_{ij}}}(-s_{ij})\mathbf{V}^i_{qn}\left(\hat{k}\right)J_n + \hat{k}\times\sum_{q\notin B_p}\alpha^i_{pq}\left(k_i,\mathbf{r}_{pq}\right)\sum_{\substack{n\in G_q \\ n\subset S_{ij}}}(-s_{ij})\mathbf{V}^i_{qn}\left(\hat{k}\right)M_n\right]d^2\hat{k},\ f\in G_p,\mathbf{r}_f\in R_i \tag{7}$$

In this expression S^2 denotes the unit (Ewald's) sphere. B_p are the indexes of the nearby groups to the observation group *p*, for which the multipolar expansion cannot be applied. G_p are the indexes of all the elements (basis functions, testing functions, observation points) in group *p* (same applies for G_q), and $\mathbf{r}_{pq}$ is the vector from the center $\mathbf{r}_q$ of the source group *q* to the center $\mathbf{r}_p$ of the observation group *p*. $\mathbf{V}^i_{qn}$ defines the radiation pattern of the basis function $\mathbf{f}_n$ referred to the center of group *q* in region *i* and in the outgoing directions $\hat{k}$ defined by the discretization of the unit sphere:

$$\mathbf{V}^i_{qn}(\hat{k}) = \int_{\Delta_n}\left(\bar{\mathbf{I}} - \hat{k}\hat{k}\right)\cdot\mathbf{f}_n(\mathbf{r})e^{-j\mathbf{k}_i(\mathbf{r}_q-\mathbf{r})}\,dS, \tag{8}$$

where Δ_n is the spatial subdomain of the *n*-th basis function $\mathbf{f}_n$ and $\mathbf{k}_i = k_i\hat{k}$. In equation (7), α^i_{pq} is the translation operator defined as:

$$\alpha^i_{pq}\left(k_i,\mathbf{r}_{pq}\right) = \sum_{m=0}^{M}(-j)^m(2m+1)h^{(2)}_m\left(k_i r_{pq}\right)P_m\left(\hat{k}\cdot\hat{r}_{pq}\right), \tag{9}$$

where $h^{(2)}_m$ is the spherical Hankel function of the second kind, P_m denotes the Legendre polynomial of degree *m* and *M* denotes the number of multipole expansion terms. Regarding the sign s_{ij} = 1 ($i < j$); –1 ($i > j$) in equation (7), it ensures the compliance with the boundary conditions at each interface. It is assumed that $i = 1$ denotes the external region. Similarly, the magnetic near field at $\mathbf{r}_f$ is obtained as:

$$\mathbf{H}(\mathbf{r}_f) = \sum_{j\in B_i}\sum_{q\in B_p}\sum_{\substack{n\in G_q \\ n\in S_{ij}}}\left(-\frac{1}{\eta_i}s_{ij}\mathcal{L}_i(\mathbf{f}_n)M_n - s_{ij}\mathcal{K}_i(\mathbf{f}_n)J_n + \frac{1}{2}\hat{n}_{ij}\times\mathbf{f}_n J_n\right) + \sum_{j\in B_i}\left(\frac{-jk_i}{4\pi}\right)^2\int_{S^2} e^{-j\mathbf{k}_i(\mathbf{r}_f-\mathbf{r}_p)}$$
$$\left[\frac{1}{\eta_i}\sum_{q\notin B_p}\alpha^i_{pq}\left(k_i,\mathbf{r}_{pq}\right)\sum_{\substack{n\in G_q \\ n\subset S_{ij}}}(-s_{ij})\mathbf{V}^i_{qn}\left(\hat{k}\right)M_n + \hat{k}\times\sum_{q\notin B_p}\alpha^i_{pq}\left(k_i,\mathbf{r}_{pq}\right)\sum_{\substack{n\in G_q \\ n\subset S_{ij}}}(-s_{ij})\mathbf{V}^i_{qn}\left(\hat{k}\right)J_n\right]d^2\hat{k},\ f\in G_p,\mathbf{r}_f\in R_i \tag{10}$$

For the sake of clarity, a one-level MLFMA has been assumed in expressions (7) and (10). The multi-level stages will be clearly set out afterwards.

2.1 Matrix notation

Let us introduce at this point a more compact matrix notation for the electric field in (7). An analogous procedure can be followed to derive the expressions in matrix notation for the magnetic field according to (10). Without lack of generality, in the following expressions we consider the radiation of just one region *j* adjacent to region *i* in order to make the formulation clearer, so the summation operator with summation index *j* can be omitted. Then, the electric near field can be written now as:

$$\mathbf{E}(\mathbf{r}_f) = \sum_{q\in B_p}\left(-\eta_i \mathbf{L}_q^T \boldsymbol{J}_q + \mathbf{K}_q^T \boldsymbol{M}_q\right) + \mathbf{W}\mathbf{S}_{fp}\left[\mathbf{U}_\theta^T \operatorname{diag}\left\{\sum_{q\notin B_p}\boldsymbol{\alpha}_{pq}\left(\eta_i \mathbf{F}_q^\theta \boldsymbol{J}_q + \mathbf{F}_q^\phi \boldsymbol{M}_q\right)\right\}\right.$$
$$\left. + \mathbf{U}_\phi^T \operatorname{diag}\left\{\sum_{q\notin B_p}\boldsymbol{\alpha}_{pq}\left(\eta_i \mathbf{F}_q^\phi \boldsymbol{J}_q - \mathbf{F}_q^\theta \boldsymbol{M}_q\right)\right\}\right]^T, \quad f \in G_p, \mathbf{r}_f \in R_i \tag{11}$$

where $\mathbf{L}_q = \left[\mathcal{L}_i(\mathbf{f}_1), \mathcal{L}_i(\mathbf{f}_2), \ldots, \mathcal{L}_i(\mathbf{f}_{N_q})\right]^T_{N_q\times 3}$ and $\mathbf{K}_q = \left[\mathcal{K}_i(\mathbf{f}_1), \mathcal{K}_i(\mathbf{f}_2), \ldots, \mathcal{K}_i(\mathbf{f}_{N_q})\right]^T_{N_q\times 3}$ are matrices whose rows yield the contribution to the scattered fields of the N_q basis functions of group q on the interface S_{ij}, which radiates to region i through the integro-differential operators $\mathcal{L}_i$ and $\mathcal{K}_i$, respectively. $\mathbf{F}_q^{\theta,\phi} = \left[\boldsymbol{F}_{q1}^{\theta,\phi}(\hat{\boldsymbol{k}}), \boldsymbol{F}_{q2}^{\theta,\phi}(\hat{\boldsymbol{k}}), \ldots, \boldsymbol{F}_{qN_q}^{\theta,\phi}(\hat{\boldsymbol{k}})\right]_{K\times N_q}$ are the aggregation matrices for the $\hat{\boldsymbol{\theta}}$ and $\hat{\boldsymbol{\phi}}$ polarizations. The columns of $\mathbf{F}_q^{\theta,\phi}$ are the outgoing radiation patterns (plane waves with *k*-vectors) of the basis functions belonging to group q pointing to the directions given by the discretization of the Ewald's sphere, $\boldsymbol{F}_{qn}^{\theta}(\hat{\boldsymbol{k}}) = -\boldsymbol{s}_{ij}\left[\hat{\boldsymbol{\theta}}_k \hat{\boldsymbol{\theta}}_k \cdot \mathbf{V}_{qn}^i(\hat{\boldsymbol{k}}_k)\right]_{K\times 1}$ and $\boldsymbol{F}_{qn}^{\phi}(\hat{\boldsymbol{k}}) = -\boldsymbol{s}_{ij}\left[\hat{\boldsymbol{\phi}}_k \hat{\boldsymbol{\phi}}_k \cdot \mathbf{V}_{qn}^i(\hat{\boldsymbol{k}}_k)\right]_{K\times 1}$, with $\mathbf{V}_{qn}^i$ following equation (8), k = 1..K and K denoting the number of quadrature points of the Ewald's sphere discretization. The diagonal matrix $\boldsymbol{\alpha}_{pq} = \operatorname{diag}\left\{\alpha_{pq}^i(\hat{k}_k \cdot \hat{r}_{pq})\right\}_{K\times K}$ is the usual translator operator, which translates the multipolar plane wave expansions from the center of the source group q to the center of the observation group p. $\mathbf{U}_\theta$ and $\mathbf{U}_\phi$ are $K \times 3$ matrices whose rows are the cartesian components of the unitary vectors $\hat{\boldsymbol{\theta}}$ and $\hat{\boldsymbol{\phi}}$ at the quadrature points on the Ewald's sphere. These matrices perform the change from spherical to cartesian coordinates, posing the plane waves on a common reference system for integration on the Ewald's sphere. $\mathbf{S}_{fp} = \operatorname{diag}\left\{\exp\left[-j\mathbf{k}_{i,k}(\mathbf{r}_f - \mathbf{r}_p)\right]\right\}_{K\times K}$ is a matrix that shifts the incoming radiation pattern from the center $\mathbf{r}_p$ of the receiving group p to the observation point $\mathbf{r}_f$, and the row vector $\mathbf{W} = \left(-jk_i/(4\pi)\right)^2\left[\omega_k\right]_{1\times K}$ contains the weights associated to the quadrature points on the Ewald's sphere multiplied by a proper leading constant. $\boldsymbol{J}_q = \left[\boldsymbol{J}_1, \boldsymbol{J}_2, \ldots, \boldsymbol{J}_{N_q}\right]^T_{N_q\times 1}$ and $\boldsymbol{M}_q = \left[\boldsymbol{M}_1, \boldsymbol{M}_2, \ldots, \boldsymbol{M}_{N_q}\right]^T_{N_q\times 1}$ are column vectors with the (known) complex coefficients of the equivalent electric and magnetic currents expansions.

2.2 Far-field computation

A significant simplification in the obtaining of the electric and magnetic fields with MLFMA can also be achieved in far region through the proper exploitation of the far-field conditions in the algorithm stages. It is important to remark that the term far-field is not related here to the usual far-field condition of electromagnetics, but rather to scenarios where we need to compute the electromagnetic fields at observation points that are far-away from the radiating geometry in the MLFMA sense, that is, observation points that would be located in octree cells not neighboring the single radiating cell of the scatterer. Nevertheless, the recycling method of the MLFMA structure employed to compute these far-fields does not make any usual far-field assumption that allows for approximations. Under the above assumptions, the multipolar expansion of MLFMA can be applied for every observation point. Moreover, when computing far field the observation region is always $i = 1$ since all the observation points belong to the external (far) region and, therefore, $s_{ij} = 1$. Conveniently, the radiating geometry is decomposed using a conventional multilevel octree, while the observation points where the far-field is to be calculated are enclosed into groups. The observation groups have the particular but advisable feature of containing only one observation point, which coincides with the center of the group. Remarkably, these observation goups do not belong to the geometry octree, but they are centered at the observation points. This contrasts with near-field computations, in which a conventional octree is built including both the geometry and the observation points. The coincidence between center of the group and observation point leads to a simplified relation between children and parent observation groups and to a fixed number of groups, regardless of what group size is being considered. The simplification of the calculations mentioned above is clearly brought to light in the following expression of the electric far field at the observation point $\mathbf{r}_f$:

$$\mathbf{E}(\mathbf{r}_f) = \mathbf{W}\left[\mathbf{U}_\theta^T \operatorname{diag}\left\{\boldsymbol{\alpha}_{pQ} \boldsymbol{R}_Q^\theta\right\} + \mathbf{U}_\phi^T \operatorname{diag}\left\{\boldsymbol{\alpha}_{pQ} \boldsymbol{R}_Q^\phi\right\}\right]^T, \tag{12}$$

where $\boldsymbol{R}_Q^\theta$ and $\boldsymbol{R}_Q^\phi$ are the $\hat{\boldsymbol{\theta}}$ and $\hat{\boldsymbol{\phi}}$ polarizations of the outgoing radiation pattern in group Q, which comprises the complete geometry at the topmost (one-cell) level of the octree (level 0). This allows profiting from an advantageous translation scheme given by the translator operator $\boldsymbol{\alpha}_{pQ} = \operatorname{diag}\left\{\alpha_{pQ}^i(\hat{k}_k \cdot \hat{r}_{pQ})\right\}_{K^{(\theta)} \times K^{(\phi)}}$ between this single box represented by its center and the far observation groups p. Since the observation groups are centered at the observation points $\mathbf{r}_f$, it must be noted that the shift matrices $\mathbf{S}_{fp}$ are not required. Matrices $\boldsymbol{R}_Q^{\theta,\phi}$ with the plane wave expansions for the complete structure in the k-space are not calculated directly, but rather obtained from the finest level L by exponential shifting and interpolation. At level L, the outgoing radiation patterns are calculated from the equivalent electric and magnetic currents and the aggregation matrices previously defined as $\boldsymbol{R}_q^{(L),\theta} = \eta_i \mathbf{F}_q^\theta \boldsymbol{J}_q + \mathbf{F}_q^\phi \boldsymbol{M}_q$, $\boldsymbol{R}_q^{(L),\phi} = \eta_i \mathbf{F}_q^\phi \boldsymbol{J}_q - \mathbf{F}_q^\theta \boldsymbol{M}_q$. At a given level l-1, the radiation pattern of group q can be obtained by exponential shift and interpolation of the outgoing radiation patterns of its children groups c, as follows:

$$\boldsymbol{R}_q^{(l-1)\theta,\phi}(\hat{\boldsymbol{k}}) = \mathbf{B}^{(l-1),(l)} \sum_{c \in C_q} \mathbf{S}_{qc}^{(l)} \boldsymbol{R}_c^{(l)\theta,\phi}, \tag{13}$$

where C_q are the indexes of the children groups c (level l) of group q (level l–1), $\mathbf{S}_{qc}^{(l)} = \mathrm{diag}\left\{\exp\left[-jk_i\hat{k}_k^{(l)}(\mathbf{r}_q^{(l-1)} - \mathbf{r}_c^{(l)})\right]\right\}_{K^{(l)} \times K^{(l)}}$ is the shifting matrix from the center of the children groups c to the center of the parent group q and $\mathbf{B}^{(l-1),(l)}$ is the $K^{(l-1)} \times K^{(l)}$ interpolation matrix from level l to level l–1. One key point of the implementation is that the interpolation matrix between two levels is full (global interpolation/anterpolation). Using global interpolation and anterpolation ensures the validity of the plane wave expansions in the entire range of spatial directions, enabling the application of the algorithm to the calculation of the radiated field at any point, without incurring possible losses of precision due to the use of local interpolation/anterpolation algorithms. Remarkably, the (full) interpolation matrices are not always explicitly calculated, but the interpolation/anterpolation operations are speeded-up for large cells at the coarser levels by conveniently reordering operations and applying a Fourier transform, followed by a (low-cost) matrix vector product and an inverse Fourier transform [35].

At this point, there are two possible ways to proceed prior to the disaggregation process:

- Doing the anterpolation down to finer levels by simply reducing the group size and, consequently, the number of k-space directions that need to be considered for the disaggregation of the receiving information. The exponential translation can be left out since the lower level groups are referred to the same center points than the higher level groups.
- Omitting the anterpolation and directly deal with the disaggregation at the coarsest level.

Aside from the option chosen, the disaggregation of the receiving information turns into the evaluation of the field expression for each observation point $\mathbf{r}_f$, already at the very center of the relevant receiving group. After calculation, a transformation from cartesian to spherical coordinates can be straightforwardly done to keep the transversal components of the field.

It is worth mentioning that, at a difference with [29], the above procedure is not restricted to far-field conditions, but to observation points that are not neighbors (in terms of MLFMA) of the coarsest radiating cells considered. Thereby, it can be applied to expedite the calculation of fields in the intermediate radiating near-field (Fresnel) region, which is beyond the reactive near-field region but where the far-field conditions are not met.

3. Numerical results

To demonstrate the applicability and efficiency of the procedure described, the ordered array of 720 silver trigonal prism nanoparticles shown in Figure 1(a), which is similar to that of [35], has been analyzed. The nanoparticles are 1.7 nm above the plane XY and the array reaches 6787 nm along the x-axis and 6496 nm along the y-axis. Each nanoparticle presents rounded tips and rounded edges in the upper face, 50 nm-height and 126 nm-side. The trigonal prisms are symmetrically grouped together in 400 nm-diameter circumferences. The well-known Rao-Wilton-Glisson (RWG) [37] vector basis functions have been used to model the surfaces. We

have taken the optical constant of silver from [37].

The equivalent currents over the geometry surfaces have been obtained by applying an efficient implementation of MLFMA algorithm adequately combined with MoM [1, 19]. Normal incidence of a plane wave with x- and y- polarizations has been considereded. First, the main spectra of the arrangement were computed to characterize its frequency response. The average of the results corresponding to both polarizations can be observed in Figure 1(b).

(Figure 1)

The electric near field over the plane shown in Figure 1(a) has been calculated for the wavelength corresponding to the resonance of the scattering cross section, 515 nm. The plane is defined by more than 12 million observation points (3501 × 3501), therefore this is an illustrative example of a highly demanding calculation in terms of, mainly, time resources. The average of the electric field magnitudes for both polarizations is shown in Figure 2(a), being Figure 2(b) a zoom of the highlighted corner area. With this result, the generation of the SERS electromagnetic enhancement map given by the $|\mathbf{E}|^4$ approximation (no Raman shift) [30] is straightforward (Figure 2(c), showing the same zoom area as in Figure 2(b)). The simulations have been performed on a workstation with four 16-core Intel Xeon E7-8867v3, 45 MB Smart-Cache processors at 2.50GHz. Under this conditions, an execution time of 135 s has been required to obtain the electric near field for one polarization. As far as the MLFMA basic configuration parameters are concerned, a group size at the finest level L of 0.0625λ and two multilevel steps (three levels) have been used in the simulations. M = 7, 9 and 12 multipole terms have been considered in (9) from the finest to the coarsest level, respectively.

(Figure 2)

For the sake of illustrating the drastic reduction of the execution time provided by MLFMA, the electric near field involved in the result of Figure 2 has been also calculated by direct evaluation of the expression in Eq. (3). The near field has been obtained for a manageable plane with considerably fewer sample points (321 × 321). Since the accuracy level of the accelerated result obtained by MLFMA is also a key point, a measure of the error e of this approach with respect to the reference given by the direct evaluation of Eq. (3), has been calculated as:

$$e = \left\| \left| E_{MLFMA} \right| - \left| E_{ref} \right| \right\| / \left\| \left| E_{ref} \right| \right\|, \tag{14}$$

where E_{MLFMA} and E_{ref} are arrays with the magnitude of the accelerated and reference fields over the observation points. This error measure has been carried out for sets with different number of multipoles, which is a determining parameter concerning the accuracy of the method. Concretely, the number of multipoles considered in each case has been obtained by modifying the value of the parameter p in the following expressions according to the data gathered in Table 1:

$$\beta = 1.8\left(-\log_{10}(p)\right)^{2/3} \tag{15}$$

$$M^{(l)} = \left\lfloor k_0 a^{(l)} + \beta \left(k_0 a^{(l)} \right)^{1/3} \right\rfloor, \tag{16}$$

where $\lfloor \cdot \rfloor$ is the integer (floor) part. $M^{(l)}$ and $a^{(l)}$ denote the number of multipoles and the cell size at level l, respectively. Table 1 exemplifies the extent of the extreme execution time decrease achievable by resorting to MLFMA in comparison with the direct form: approximately half a minute versus almost three hours in this example.

(Table 1)

The time required for the field calculation over the plane of Figure 2 with 3501×3501 samples (approximately 119 times the number of points considered in Figure 3(b)-(d)) using the direct evaluation and with the same computation resources can be extrapolated from the example of Table 1. The extrapolation results in an estimated time of 13.4 days, while the same result addressed by MLFMA took 135 seconds, showing that the benefits of a well-designed MLFMA parallelization strategy are more visible as the problem size grows. The acceleration obtained makes clear that this is an efficient and highly scalable implementation, which takes maximum advantage of the available computational resources. Although in this work we had access to high-performing computing machines, we herein also considered a typical scenario with less powerful resources. In that context, the reduction of the execution time brought about by the presented MLFMA implementation for the extraction of near and far fields would become crucial. For example, using a more modest workstation with two 8-core Intel(R) Xeon(R) CPU E7- 4820 @ 2.00GHz, 500 GB RAM processors, MLFMA would take 256 seconds for the largest plane, while the computing time of the direct evaluation would change from the aforementioned 13 days to almost 3 months, which could be completely unacceptable depending on the circumstances.

Figure 3 depicts the accuracy of our implementation when dealing with the calculation of near fields. Figure 3(a) shows the error versus the parameter p (and, consequently, versus $M^{(l)}$), and Figure 3(b)-(d) allows for a comparison between the reference result and the worst/best cases in terms of expected accuracy given by the highest and the lowest value of p in Table 1, respectively. Despite the error values of Figure 3(a) being moderate, Figure 3(b) shows that the simulation result with the lowest $M^{(l)}$ (the highest p) corresponds, obviously, to an inadequate configuration of the method for the pursued result, since the octree tesselations can be clearly appreciated. Nevertheless, it can be also observed that the resolution of the field representation improves clearly when the number of multipoles is increased. It must be noted that MLFMA is error-controllable and, as such, the approximation degree, so vital in near field calculations, can be straightforwardly managed through the parameter p; importantly, this can be done without a significant impact on the total running time. Our experience points out that values of $M^{(l)}$ slightly higher than those typically employed to get the surface currents (p around 10^{-8} or 10^{-10}) are enough to obtain a satisfactory near field result.

(Figure 3)

Finally, as an example of far-field calculations, we obtained, for the same resonant scenario of Figure 2 and Figure 3, the differential scattering cross section σ_d [33] for three planes cuts with

1441 observation points each. The results for the three cuts have been sequentially obtained in a single simulation and they are shown in Figure 4. σ_d is defined as the scattering cross section, σ_s, per unit solid angle. It is thus an angular function (θ and ϕ dependence) with dimensions of area per unit solid angle:

$$\sigma_d = \frac{d\sigma_s}{d\Omega}. \tag{17}$$

σ_s is calculated from the incident and scattered fields, $\mathbf{E}_i$, $\mathbf{H}_i$ and $\mathbf{E}_s$, $\mathbf{H}_s$, respectively, as:

$$\sigma_s = \frac{\oint_{S_0} \frac{1}{2}\mathrm{Re}\left(\mathbf{E}_s \times \mathbf{H}_s^*\right) d\mathbf{S}}{\frac{1}{2}\left|\mathrm{Re}\left(\mathbf{E}_i \times \mathbf{H}_i^*\right)\right|}, \tag{18}$$

where S_0 is an arbitrary closed surface enclosing the array, $d\mathbf{S}$ is a vector representing the differential surface area directed outward, and * is the complex conjugate. A group size at the finest level L of 0.125λ and seven multilevel steps (eight levels) have been considered. $M^{(l)}$ has been calculated according to (16) with $p = 10^{-3}$ in (15).

(Figure 4)

The MLFMA simulation has supplied the results in 8.11 seconds, in contrast with the 217.56 seconds required for the computation of the electric field following the expression (3). The error of Eq. (14) as well as a similar error measure defined for the complex transversal components of the electric field are compiled in Table 2. The reference stays the same, the electric field evaluated according to (3). As expected, these error values are lower than those obtained when computing near field. Near radiation is a more demanding calculation, which entails the necessity of a more careful configuration of the method.

(Table 2)

4. Summary

An efficient implementation of MLFMA has been used for the calculation of usually demanded post-processing results such as near and far fields, which are time-consuming if direct evaluation is used. As it can be extracted from the detailed formulation exposed, the application of the method requires an adequate strategy for organizing the computations involved in the extraction of the near and far fields. Our implementation has demonstrated to be efficient and highly scalable, thereby squeezing the available resources to the maximum extent.

The numerical results included in this work have distinctly pointed out the drastic speed-up of the execution time that can be attained by using MLFMA in the calculation of radiated fields, as compared to the direct form given by the Straton-Chu formulas. Indeed, the acceleration in the calculation of the electromagnetic fields can turn into a deciding issue throughout the development of a project depending on what kind of computational resources are available, time constraints, etc. More importantly, this speed-up takes place in an error-controllable

fashion, and thus sufficiently accurate results can still be rendered by MLFMA as long as its key parameters are properly configured.

References

1. Song JM, Chew WC. Multilevel fast multipole algorithm for solving combined field integral equations of electromagnetic scattering. Microw. Opt. Tech. Lett. 1995;10:14-19.
2. Song J, Lu C-C, Chew WC. Multilevel fast multipole algorithm for electromagnetic scattering by large complex objects. IEEE Trans. Antennas Propag. 1997;45(10):1488–1493.
3. Donepudi KC, Jin J-M, Chew WC. A higher order multilevel fast multipole algorithm for scattering from mixed conducting/dielectric bodies. IEEE Trans. Antennas Propag. 2003;51(10):2814–2821.
4. Chew, WC, Jin J-M, Michielssen E, et al. Fast and Efficient Algorithms in Computational Electromagnetics. Boston, MA: Artech House; 2001.
5. Harrington RF. Field Computation by Moment Method. NY: IEEE Press; 1993.
6. Ergül Ö, Gürel L. Efficient parallelization of the multilevel fast multipole algorithm for the solution of large-scale scattering problems. IEEE Trans. Antennas Propag. 2008;56:2335–2345.
7. Ergül Ö, Gürel L. A hierarchical partitioning strategy for an efficient parallelization of the multilevel fast multipole algorithm. IEEE Trans. Antennas Propag. 2009;57:1740–1750.
8. Araújo MG, Taboada JM, Obelleiro F, et al. Supercomputer aware approach for the solution of challenging electromagnetic problems, Progress In Electromagn. Res. 2010;101:241–256.
9. Taboada JM, Araújo MG, Bértolo JM, et al. MLFMA-FFT parallel algorithm for the solution of large-scale problems in electromagnetics. Progress In Electromagn. Res. 2010;105:15-30.
10. Ergül Ö, Gürel L. Rigorous solutions of electromagnetic problems involving hundreds of millions of unknowns. IEEE Antennas Propag. Mag. 2011;53(1):18–27.
11. Taboada JM, Araújo MG, Obelleiro F, et al. MLFMA-FFT parallel algorithm for the solution of extremely large problems in electromagnetics (INVITED PAPER). Proc. IEEE 2013;101(2):350–363.
12. Myroshnychenko V, Rodriguez-Fernandez J, Pastoriza-Santos I, et al. Modelling the optical response of gold nanoparticles, Chem. Soc. Rev. 2008;37(9):1792-1805.

13. Rivero J,Taboada JM, Landesa L, et al. Surface integral equation formulation for the analysis of left-handed metamaterials. Optics Express 2010;18:15876-15886.
14. Gallinet B, Martin OJF, Scattering on Plasmonic Nanostructures Arrays Modeled with a Surface Integral Formulation. Photonic Nanostruct. 2010;8:278–284.
15. Gallinet B, Kern AM, Martin OJF. Accurate and Versatile Modeling of Electromagnetic Scattering on Periodic Nanostructures with a Surface Integral Approach. J. Opt. Soc. Am. A 2010;27:2261– 2271.
16. Taboada JM, Rivero J, Obelleiro F, ET AL. Method-of-moments formulation for the analysis of plasmonic nano-optical antennas. J. Opt. Soc. Am. A 2011;28:1341-1348.
17. Gallinet B, Siegfried T, Sigg H, et al. Plasmonic Radiance: Probing Structure at the Ångström Scale with Visible Light. Nano Lett. 2013;13(2):497–503.
18. D. M. Solís, J. M. Taboada, F. Obelleiro, L. M. Liz-Marzán, and F. J. García de Abajo, Toward ultimate nanoplasmonics modeling, ACS Nano 8(8) (2014) 7559-7570.
19. Solís DM, Araújo MG, Landesa L, et al. MLFMA-MoM for Solving the Scattering of Densely Packed Plasmonic Nanoparticle Assemblies. IEEE Phot. J. 2015;7(3):4800709.
20. Yilmaz A, Karaosmanoğl B, Ergül Ö. Computational Electromagnetic Analysis of Deformed Nanowires Using the Multilevel Fast Multipole Algorithm. Sci. Rep. 2015;5:8469.
21. Farrokhtakin E, Rodríguez-Fernández D, Mattoli V, et al. Radial Growth of Plasmon Coupled Gold Nanowires on Colloidal Templates. Journal of Colloid and Interface Science 2015;449:87-91.
22. Fernández-López C, Polavarapu L, Solís DM, et al. Gold Nanorods-pNIPAM hybrids with Reversible Plasmon Coupling: Synthesis, Modeling and SERS properties. ACS Applied Materials & Interfaces 2015;7(23):12530-12538.
23. Shiohara A, Novikov SM, Solís DM, et al. Plasmon Modes and Hot Spots in Gold Nanostar–Satellite Clusters. Journal of Physical Chemistry C 2015;119(20):10836-10843.
24. Hamon C, Novikov S, Scarabelli L, et al. Collective Plasmonic Properties in Few-Layer Gold Nanorod Supercrystals. ACS Photonics 2015;2(10):1482-1488.
25. Gallinet B, Butet J, Martin OJF, Numerical methods for nanophotonics: standard problems and future challenges. Laser Photonics Rev. 2015;9(6):577–603.
26. Sánchez-Iglesias A, Barroso J, Solís DM, et al. Plasmonic Substrates Comprising Gold Nanostars efficiently regenerate cofactor molecules. Journal of Materials Chemistry A 2016;4:7045-7052.

27. Solís DM, Taboada JM, Obelleiro F, et al. Optimization of Nanoparticle-Based SERS Substrates through Large-Scale Realistic Simulations. ACS Photonics 2017; 4(2): 329-337.
28. Velamparambil S, Chew WC, and Song J, 10 million unknowns: is it that big?. IEEE Antennas and Propagation Magazine 2003; 45(2): 43-58.
29. Tzoulis A and Eibert TF, Efficient electromagnetic near-field computation by the multilevel fast multipole method employing mixed near-field/far-field translations. IEEE Antennas and Wireless Propagation Letters 2005; 4: 449-452.
30. Novotny L, Hecht B. Principles of Nano-Optics. Cambridge: Cambridge Univ. Press; 2006.
31. Schlücker S. Surface-enhanced raman spectroscopy: Concepts and chemical applications. Agew. Chem. Int. Ed. 2014;53:4756–4795.
32. Bohren CF, Huffman DR. Absorption and Scattering of Light by Small Particles. NY: John Wiley; 1983.
33. Ishimaru A. Electromagnetic Wave Propagation, Radiation and Scattering. NJ: Prentice-Hall; 1991.
34. Gumerov A, Duraiswami R, Borovikov EA. Data Structures, Optimal Choice of Parameters, and Complexity Results for Generalized Multilevel Fast Multipole Methods in d Dimensions. Baltimore: Comput. Sci. Dep., Univ. Maryland; 2003 (Tech. Rep. CS-TR-4458 UMIACS; UMIACS-TR-2003-28).
35. Sylvand G. La méthode multipôle rapide en électromagnétisme: performances, parallélisation, applications [Ph.D. dissertation]. Paris: ENPC Paris; 2002.
36. Haes AJ, van Duyne RP. A unified view of propagating and localized surface plasmon resonance biosensors. Anal. Bioanal Chem. 2004;379:920–930.
37. Rao SM, Wilton DR, Glisson AW. Electromagnetic scattering by surfaces of arbitrary shape. IEEE Trans. Antennas Propag. 1982;30(3):409-418.
38. Palik, ED. Handbook of Optical Constants of Solids. NY: Academic Press; 1985.

Tables with Captions

Table 1. Execution time to obtain the electric near field (one polarization) for 321 × 321 sample observation points when using MLFMA with different number of multipoles and direct evaluation of Eq. (3).

MLFMA			Direct evaluation
p	$M^{(l)}$	Ex. time (s)	Ex. time (s)
10^{-14}	[8 10 13]	34.2	9720.3 (~ 2.7 h)
10^{-12}	[7 9 12]	28.6	
10^{-10}	[6 8 11]	25.6	
10^{-8}	[5 7 9]	25.3	
10^{-6}	[4 6 8]	24.8	

Table 2. Error in the far field calculation with MLFMA with regard to direct evaluation of Eq. (3).

	x-pol			y-pol		
	XY-plane	XZ-plane	YZ-plane	XY-plane	XZ-plane	YZ-plane
$\left\| E^{\theta}_{MLFMA} - E^{\theta}_{ref} \right\| / \left\| E^{\theta}_{ref} \right\|$	$2.22 \cdot 10^{-3}$	$1.85 \cdot 10^{-3}$	$1.99 \cdot 10^{-3}$	$2.36 \cdot 10^{-3}$	$1.69 \cdot 10^{-3}$	$1.74 \cdot 10^{-3}$
$\left\| E^{\phi}_{MLFMA} - E^{\phi}_{ref} \right\| / \left\| E^{\phi}_{ref} \right\|$	$1.82 \cdot 10^{-3}$	$1.70 \cdot 10^{-3}$	$1.71 \cdot 10^{-3}$	$1.84 \cdot 10^{-3}$	$1.79 \cdot 10^{-3}$	$1.70 \cdot 10^{-3}$
e of Eq. (14)	$0.70 \cdot 10^{-4}$	$0.87 \cdot 10^{-4}$	$0.38 \cdot 10^{-4}$	$0.66 \cdot 10^{-4}$	$0.86 \cdot 10^{-4}$	$0.79 \cdot 10^{-4}$

Figure Captions

Figure 1. (a) Geometry used in the simulations and plane used for the subsequent calculation of the electric near field. The nanoparticles are 1.7 nm above the XY-plane and the plane for computing the near field is placed at z = 25 nm. A zoom of one nanoparticle is shown in the inset: each nanoparticle presents rounded tips and rounded edges in the upper face, 50 nm-height and 126 nm-side. (b) Cross sections (nm^2) of the arrangement of Figure1(a).

Figure 2. Electric near field computations at λ = 515 nm over the red plane of 3501×3501 points shown in Figure1(a). (a) Average of the electric field magnitudes corresponding to x- and y- polarizations. (b) Zoom of Figure2(a). (c) SERS enhancement map given by the $|\mathbf{E}|^4$ approximation corresponding to the arrangement of Figure 1.

Figure 3. (a) Normalized error of the electric near field computed by MLFMA with respect to the electric near field given by the direct evaluation of Eq. (3). (b)-(d) Magnitude of the electric near field (average of x- and y- polarizations) in the vicinity of one nanoparticle calculated by (b) MLFMA with $p = 10^{-6}$, (c) MLFMA with $p = 10^{-14}$ and (d) direct evaluation of Eq. (3).

Figure 4. (a) Direction and polarization of the plane wave inciding on the nanoparticles array. (b)-(d) Differential scattering cross section ($dBnm^2/sr$) of the arrangement for x- and y-polarizations and for: (b) XY-plane, (c) XZ-plane and (d) YZ-plane.

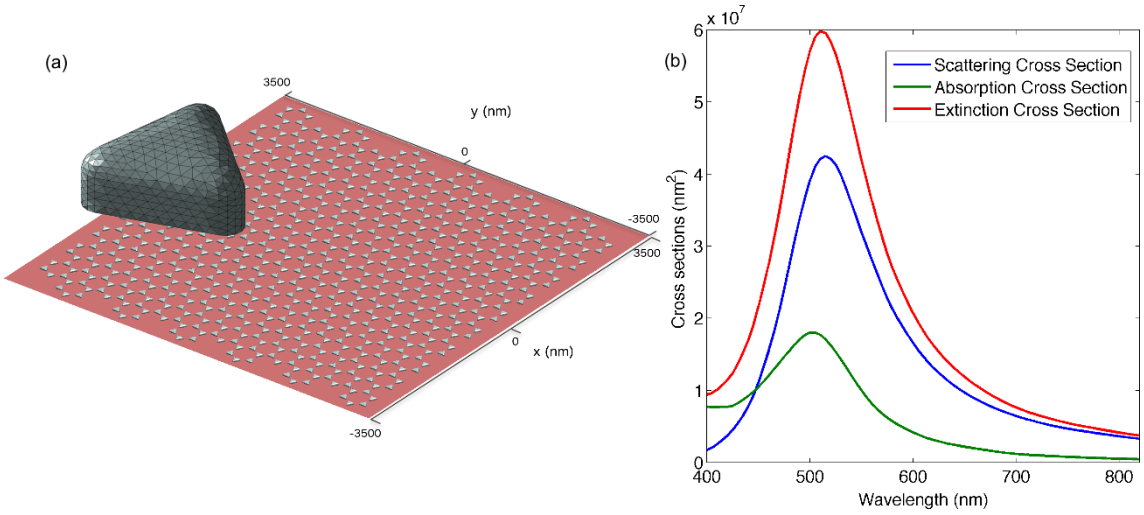

Figure 1. (a) Geometry used in the simulations and plane used for the subsequent calculation of the electric near field. The nanoparticles are 1.7 nm above the XY-plane and the plane for computing the near field is placed at z = 25 nm. A zoom of one nanoparticle is shown in the inset: each nanoparticle presents rounded tips and rounded edges in the upper face, 50 nm-height and 126 nm-side. (b) Cross sections (nm2) of the arrangement of Figure 1(a)

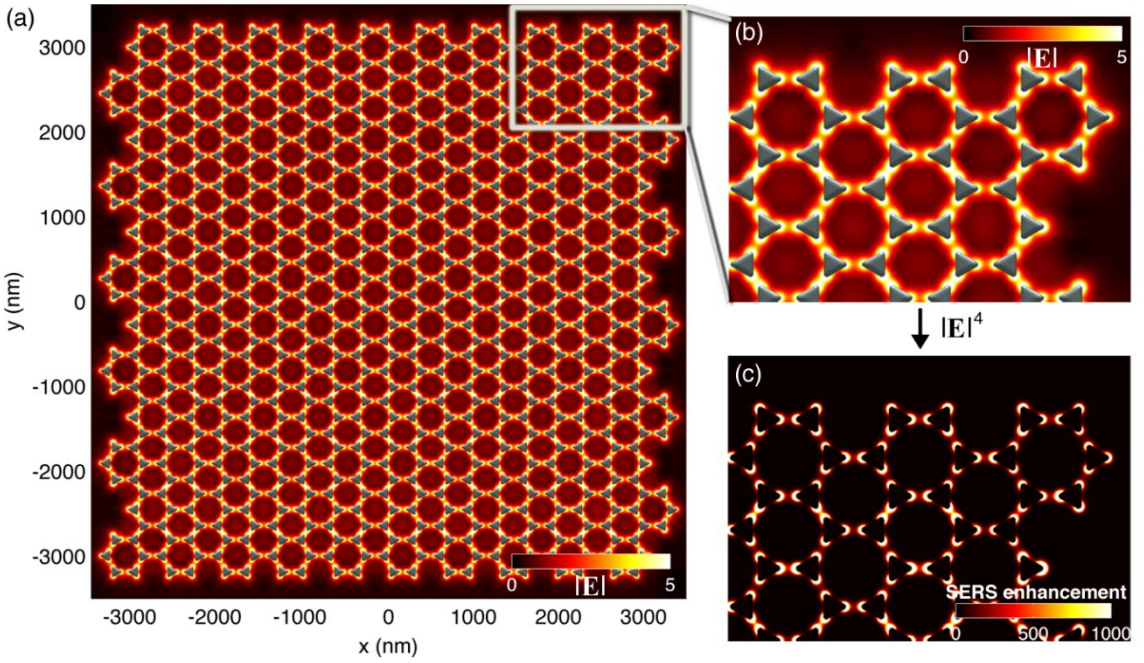

Figure 2. Electric near field computations at λ = 515 nm over the red plane of 3501 × 3501 points shown in Figure 1(a). (a) Average of the electric field magnitudes corresponding to x- and y-polarizations. (b) Zoom of Figure 2(a). (c) SERS enhancement map given by the $|E|^4$ approximation corresponding to the arrangement of Figure 1.

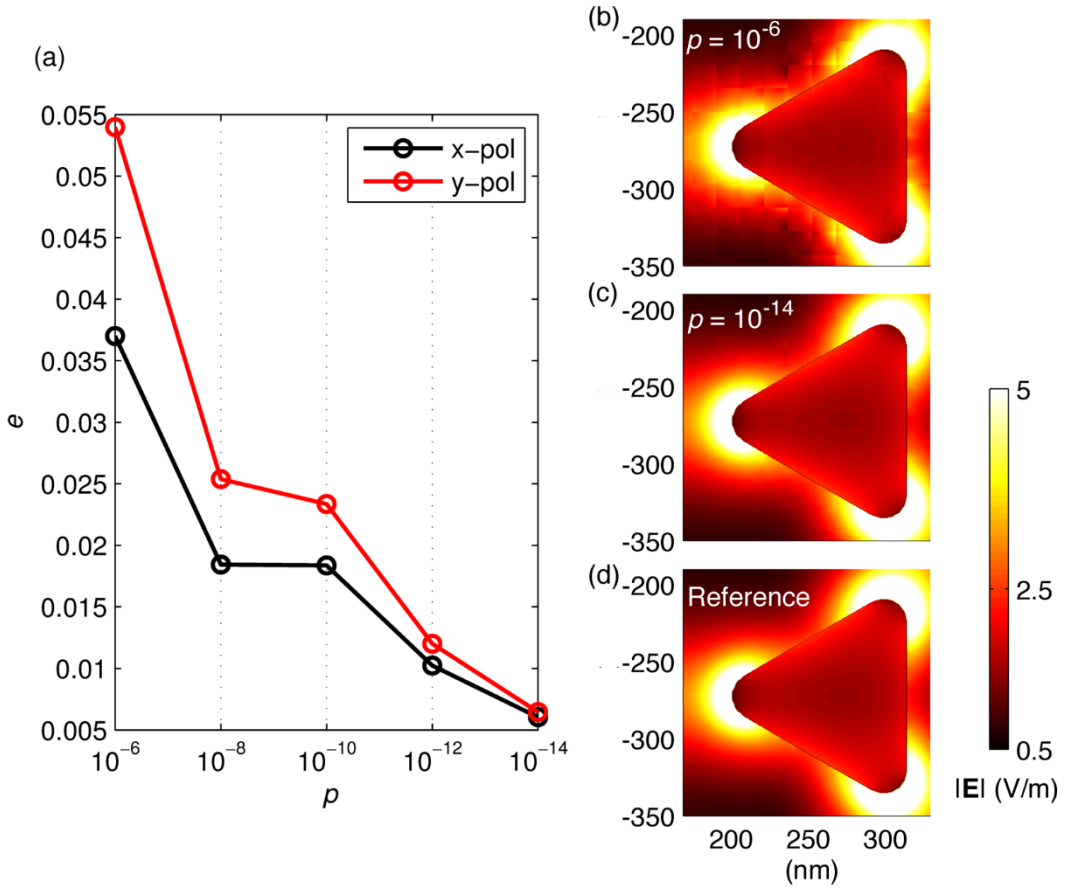

Figure 3. (a) Normalized error of the electric near field computed by MLFMA with respect to the electric near field given by the direct evaluation of Equation (3). (b)–(d) Magnitude of the electric near field (average of x- and y- polarizations) in the vicinity of one nanoparticle calculated by (b) MLFMA with p = 10−6, (c) MLFMA with p = 10−14, and (d) direct evaluation of Equation (3).

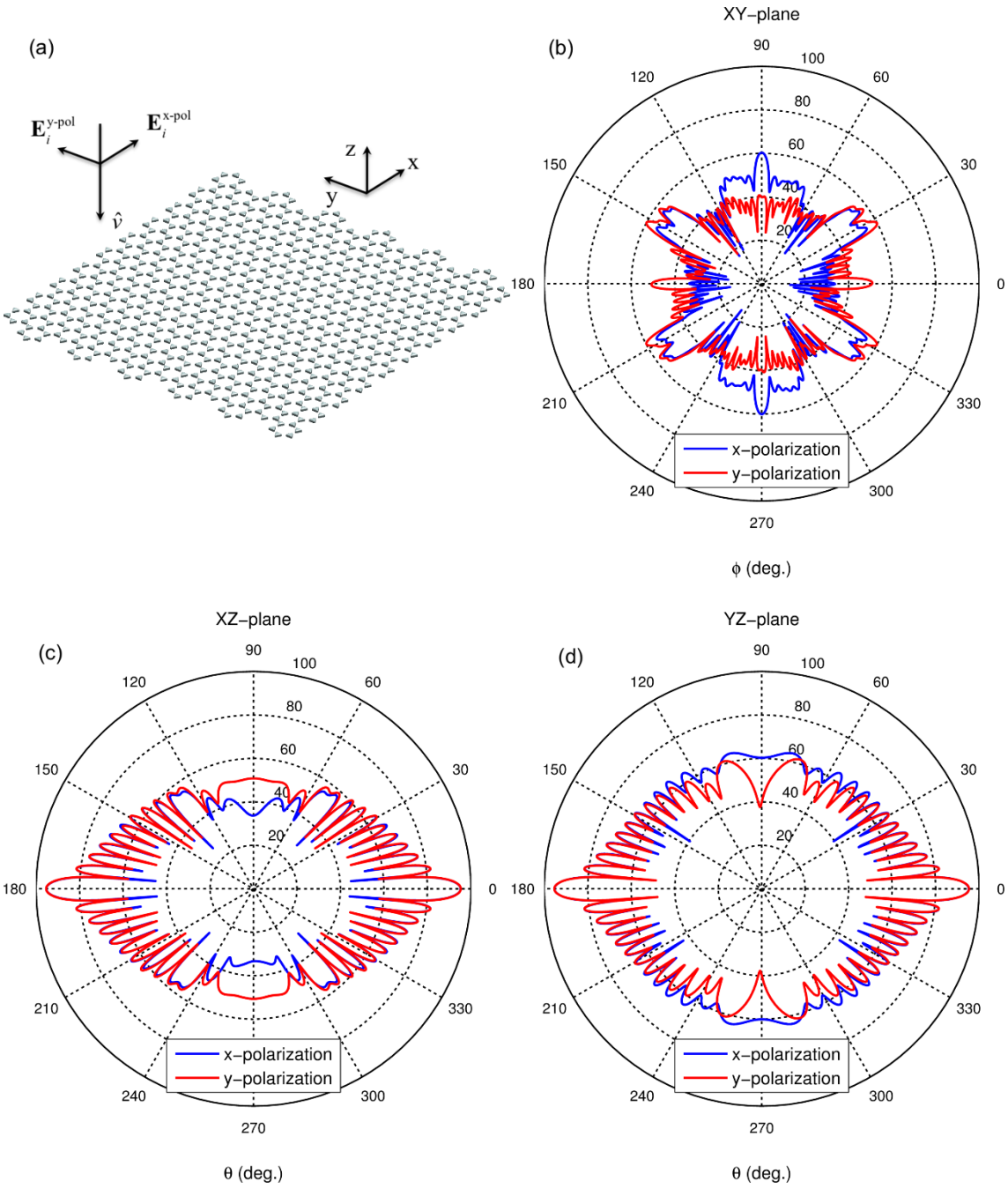

Figure 4. (a) Direction and polarization of the plane wave inciding on the nanoparticles array. (b)–(d) Differential scattering cross section (dBnm2 /sr) of the arrangement for x- and y-polarizations and for: (b) XY-plane, (c) XZ-plane, and (d) YZ-plane.